https://doi.org/10.1038/s41586-019-1180-9

Three-dimensional quantum Hall effect and metal–insulator transition in $ZrTe_5$

Fangdong Tang[1,8], Yafei Ren[2,8], Peipei Wang[1], Ruidan Zhong[3], John Schneeloch[3], Shengyuan A. Yang[4]*, Kun Yang[5,6], Patrick A. Lee[7], Genda Gu[3], Zhenhua Qiao[2]* & Liyuan Zhang[1]*

The discovery of the quantum Hall effect (QHE)[1,2] in two-dimensional electronic systems has given topology a central role in condensed matter physics. Although the possibility of generalizing the QHE to three-dimensional (3D) electronic systems[3,4] was proposed decades ago, it has not been demonstrated experimentally. Here we report the experimental realization of the 3D QHE in bulk zirconium pentatelluride ($ZrTe_5$) crystals. We perform low-temperature electric-transport measurements on bulk $ZrTe_5$ crystals under a magnetic field and achieve the extreme quantum limit, where only the lowest Landau level is occupied, at relatively low magnetic fields. In this regime, we observe a dissipationless longitudinal resistivity close to zero, accompanied by a well-developed Hall resistivity plateau proportional to half of the Fermi wavelength along the field direction. This response is the signature of the 3D QHE and strongly suggests a Fermi surface instability driven by enhanced interaction effects in the extreme quantum limit. By further increasing the magnetic field, both the longitudinal and Hall resistivity increase considerably and display a metal–insulator transition, which represents another magnetic-field-driven quantum phase transition. Our findings provide experimental evidence of the 3D QHE and a promising platform for further exploration of exotic quantum phases and transitions in 3D systems.

The QHE has been intensively investigated in two-dimensional (2D) systems, where the Hall conductivity σ_{xy} takes quantized values of $\nu e^2/h$ while the longitudinal conductivity σ_{xx} vanishes. Here, ν is the Landau level filling factor, e is the elementary charge and h is Planck's constant. Since the discovery of the 2D QHE, the possibility of extending this effect to 3D systems has been speculated, and in a seminal work Halperin[3] proposed signatures for such a 3D QHE: the Fermi level must lie in an energy gap such that $\sigma_{xx} = 0$ and the Hall conductivity must satisfy

$$\sigma_{xy} = \frac{e^2}{2\pi h} G_z \tag{1}$$

where G_z is the z-component of a reciprocal lattice vector corresponding to the period of the 3D system along the magnetic field, $\boldsymbol{B}$. This period could correspond either to the lattice structure[5] or—in more interesting cases, such as the one reported here—to superstructure arising from interaction effects.

To realize the QHE in three dimensions, the most straightforward strategy is to stack 2D QHE layers along the z axis, as has been demonstrated in semiconductor multilayer superlattices[6]. However, such systems are still of 2D nature (often referred to as 'quasi-2D' systems). Here, quasi-2D and 3D systems are distinguished by their Fermi surface topology: whereas for quasi-2D systems the Fermi surface is open along the stacking direction, it is closed for 3D systems (see Methods for further discussion). Much effort has been devoted to searching for the 3D QHE, for example, in inorganic Bechgaard salts[7,8], η-Mo_4O_{11}[9], n-doped Bi_2Se_3[10] and $EuMnBi_2$[11]. However, the essential signature of the 3D QHE—that is, a quantized Hall resistivity ρ_{xy} and vanishing longitudinal resistivity ρ_{xx}—has not been observed. Moreover, the above material systems did not show in-plane quantum oscillations, which suggests that they are probably quasi-2D systems.

$ZrTe_5$ is a promising platform for investigating the 3D QHE. It has an orthorhombic layered structure with space group *Cmcm* (number 63), as shown in Fig. 1a, where the three principal crystal axes a, c and b correspond to the directions x, y and z, respectively. Previous experiments and first-principles calculations have shown that its conduction and valence bands nearly touch at the Γ point[12]. In addition, $ZrTe_5$ has been studied in the past for its unusual thermoelectric properties[13] and possible nontrivial band topology[12,14–17].

Our experiment was performed on four different bulk $ZrTe_5$ samples, with qualitatively similar results. Hereafter we focus mainly on sample 2. The inset of Fig. 1b illustrates the setup of our transport measurement. It has the standard Hall bar geometry, with current I running along x through a 3D bulk $ZrTe_5$ sample. We first characterized the transport property in a wide temperature range of $T = 0.6$–200 K at zero magnetic field. The temperature dependence of the resistivity $\rho_{xx}(T) = \frac{Wd}{L} R_{xx}(T)$ is shown in Fig. 1b. Here W, L and d denote the width, length and thickness, respectively, of the sample, as defined in the longitudinal and Hall transport measurement, and R_{xx} is the longitudinal resistance. One clearly observes an anomalous peak around $T_p \approx 95$ K, which is attributed to a transition of carrier type. This is further verified by low-magnetic-field Hall measurements (Fig. 1c), from which we extract the density $\left(n = \frac{dB}{|e|\, d\rho_{xy}}\right)$ and mobility $\left(\mu = \frac{1}{|e|\, \rho_{xx} n}\right)$ of the dominant carrier as functions of the temperature. As shown in Fig. 1d, the mobility is extremely high at low temperature, about 10^5 cm^2 V^{-1} s^{-1} at 0.6 K, and decreases rapidly as temperature increases. Notably, the carrier density changes sign around T_p, which indicates that the system is transformed from an 'electron-type' metal below T_p to a 'hole-type' insulator above T_p. This observation is consistent with previous ARPES measurements[18]. In the following, we focus on the low-temperature regime, where the transport is dominated by electron carriers.

We probe the morphology of the Fermi surface using Shubnikov–de Haas (SdH) oscillations at 1.5 K. We rotate the direction of the applied $\boldsymbol{B}$ field with respect to the crystal axes and measure the SdH oscillations in a series of rotation angles. Figure 2a shows the results for a magnetic field $\boldsymbol{B}$ along the three principal directions x, y and z.

---

[1]Department of Physics and Shenzhen Institute for Quantum Science and Engineering, Southern University of Science and Technology, Shenzhen, China. [2]International Center for Quantum Design of Functional Materials, Hefei National Laboratory for Physical Sciences at the Microscale and Synergetic Innovation Centre of Quantum Information and Quantum Physics, CAS Key Laboratory of Strongly Coupled Quantum Matter Physics, and Department of Physics, University of Science and Technology of China, Hefei, China. [3]Condensed Matter Physics and Materials Science Department, Brookhaven National Laboratory, Upton, NY, USA. [4]Research Laboratory for Quantum Materials, Singapore University of Technology and Design, Singapore, Singapore. [5]Department of Physics, Florida State University, Tallahassee, FL, USA. [6]National High Magnetic Field Laboratory, Florida State University, Tallahassee, FL, USA. [7]Department of Physics, Massachusetts Institute of Technology, Cambridge, MA, USA. [8]These authors contributed equally: Fangdong Tang, Yafei Ren. *e-mail: shengyuan_yang@sutd.edu.sg; qiao@ustc.edu.cn; zhangly@sustech.edu.cn

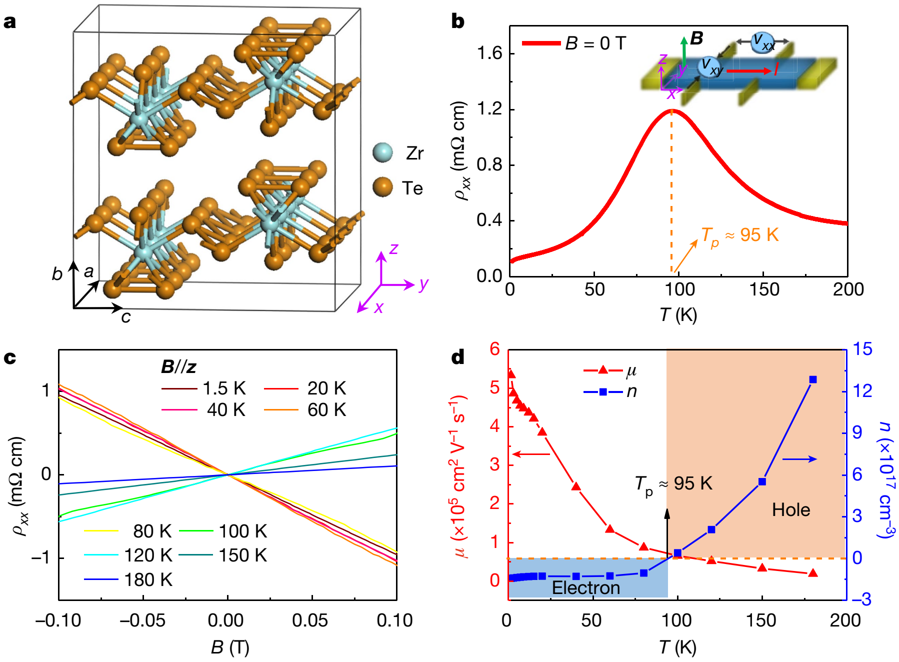

Fig. 1 | Temperature dependence of transport properties. a, Crystal structure of $ZrTe_5$. **b**, Temperature dependence of the longitudinal resistivity $\rho_{xx}(T)$ at zero magnetic field. The anomalous resistance peak occurs around $T_p \approx 95$ K. The inset shows the $ZrTe_5$ sample (green) with the Hall bar contact, where V_{xx} is the longitudinal voltage and V_{xy} the transverse Hall voltage. **c**, Temperature dependence of the Hall resistivity of $ZrTe_5$. **d**, Temperature dependence of the mobility, μ, and carrier density, n, of the dominant carrier. A transition from electron- to hole-dominated transport is observed around temperature T_p.

We observe that the oscillations start at very small fields, at $B_{int} \approx 0.067$ T, which indicates the extremely high mobility of the sample.

The frequency of the SdH oscillation ($B_{F,i}$) is determined by the extremal cross-sectional area ($S_{F,i}$) of the Fermi surface that is normal to the field direction, via the Onsager relation, $B_{F,i} = S_{F,i}\left(\frac{\hbar}{2\pi e}\right)$, where i denotes the field direction. In our measurement, we find only a single dominant frequency for each field direction, consistent with the picture of a single electron pocket with a regular convex shape. The extracted oscillation frequencies for $\boldsymbol{B}$ along the three principal directions are $B_{F,x} = 15.7 \pm 0.2$ T, $B_{F,y} = 9.2 \pm 0.1$ T and $B_{F,z} = 1.18 \pm 0.02$ T. As shown in Fig. 2e, assuming an ellipsoidal Fermi surface, which is reasonable for orthorhombic crystal symmetry and low carrier density, we have $S_{F,z} = \pi k_{F,x} k_{F,y}$, where $k_{F,i}$ is the Fermi wave-vector along

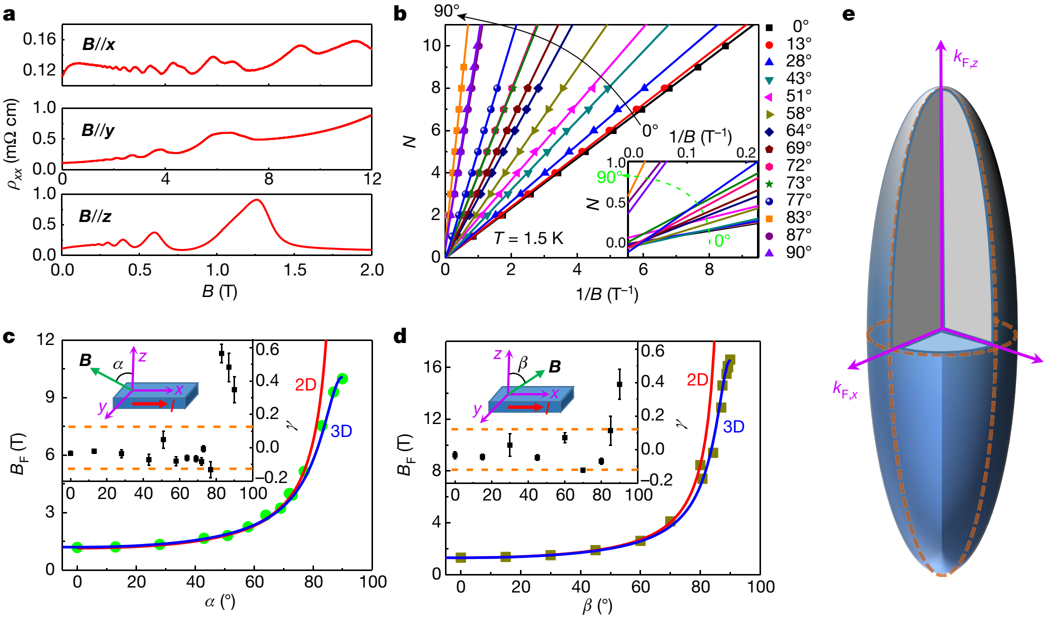

Fig. 2 | Topology and morphology of the Fermi surface in $ZrTe_5$. a, Quantum SdH oscillation with the magnetic field $\boldsymbol{B}$ parallel to the x, y and z axes for longitudinal resistivity $\rho_{xx}(B)$. **b**, Landau fan diagram of the Landau level index N versus $1/B$ for different angles β in the x–z plane (see inset of **d**; the angle β between z and $\boldsymbol{B}$ is positive from the z direction to the x direction). The inset shows a zoom-in of the main plot at low N, $1/B$ values. **c**, **d**, Angle dependence of oscillation frequency B_F as a function of angle α (**c**) and β (**d**). The red fitting curves represent the planar 2D Fermi surface, and the blue fitting curves correspond to a 3D ellipsoidal Fermi surface. The insets show the angle dependence of the intercept γ of the Landau fan diagram with error bars and schematic illustrations of the sample and external magnetic field. All error bars are one standard deviation. **e**, Topology and morphology of the Fermi surface of $ZrTe_5$ in momentum space, showing $k_{F,x}$, $k_{F,y}$ and $k_{F,z}$.

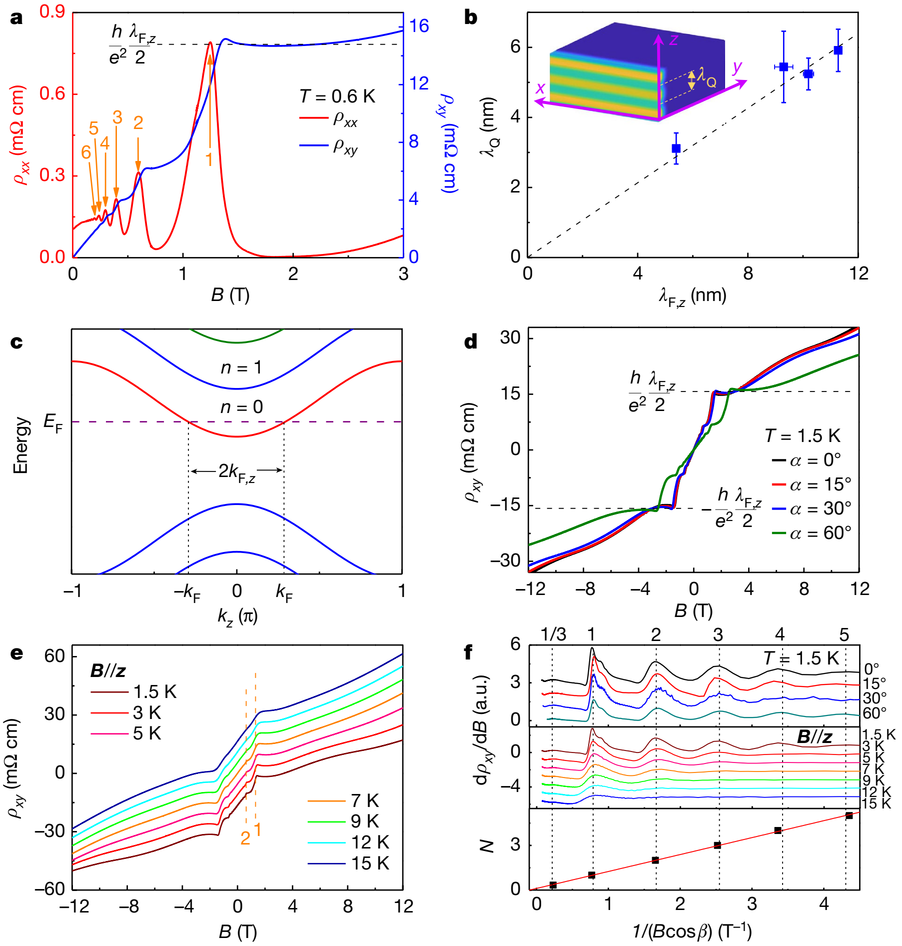

Fig. 3 | 3D QHE and transport signatures of edge states. a, Longitudinal resistivity, $\rho_{xx}(B)$ (red, left axis) and Hall resistivity $\rho_{xy}(B)$ (blue, right axis) as a function of magnetic field at temperature 0.6 K. **b**, Period of the CDW state, λ_Q, versus Fermi wavelength, $\lambda_{F,z}$, in the z direction. The inset shows a schematic of CDW. Error bars are one standard deviation. **c**, Landau-level dispersion along the z direction as a function of Fermi wave-vector. **d**, Hall resistivity $\rho_{xy}(B)$ as a function of magnetic field applied along different directions with angle α (see inset of Fig. 2c; α is positive from the z direction to the x direction). **e**, Hall resistivity ρ_{xy} as a function of magnetic field for different temperatures. Lines with similar temperatures are shifted by 5 mΩ cm for clarity. **f**, Top, $d\rho_{xy}(B)/dB$ versus $1/B_\perp$ for magnetic fields along directions with angles $\beta = 0°, 15°, 30°, 60°$ with $B_\perp = \cos\beta$. Middle, $d\rho_{xy}(B)/dB$ versus $1/B_\perp$ at different temperatures. Bottom, Landau fan diagram of Landau index N versus $1/B_\perp$. a.u., arbitrary units. The vertical dashed lines in **e** and **f** show the corresponding filling factor ν. The orange numbers in **a**, **e** denote the filling factor ν.

the i direction, and similar relations hold for $S_{F,x}$ and $S_{F,y}$. Thus, from the SdH oscillation, one can readily extract the three Fermi wave-vectors $k_{F,i}$ ($i = x, y, z$). Their values are listed in Extended Data Table 1. The result shows that the pocket is quite small, indicating ultra-low carrier density.

Because $k_{F,z}$ is a crucial factor in the following discussion, we also estimate its value using an alternative approach. The bulk carrier density n_{3D} is determined by a low-field Hall measurement, and in our case it is related to the Fermi wave-vectors via $n_{3D} = k_{F,x}k_{F,y}k_{F,z}/(3\pi^2)$. Hence, $k_{F,z}$ can be obtained as $k_{F,z} = 3\pi^2 n_{3D}\hbar/(2eB_{F,z})$. For sample 2, this approach gives a value of $k_{F,z} \approx 0.056 \pm 0.001$ Å^{-1}, which agrees well with the value of about 0.061 ± 0.004 Å^{-1} obtained solely from the SdH measurements. This in turn supports that the pocket has a closed ellipsoidal shape.

In Fig. 2b, via standard Landau-level fan diagram analysis, we obtain the SdH oscillation frequency B_F versus the tilt angles α and β, as plotted in Fig. 2c, d. We fit the data with two different formulas. One is for a 2D cylindrical Fermi surface with $B_F^{2D} = B_{F,z}/\cos\theta$ (red curve), and the other is for a 3D ellipsoidal Fermi surface with $B_F^{3D} = B_{F,z}B_{F,i}/\sqrt{(B_{F,z}\sin\theta)^2 + (B_{F,i}\cos\theta)^2}$, where $\theta = \{\alpha, \beta\}$ and $i = \{x, y\}$. The data are well fitted by the 3D formula but deviate considerably from the 2D one for $\theta > 75°$.

Having confirmed the 3D character of the system, we focus on the intermediate field range $B \approx 0$–3 T along the z direction. A zoom-in plot for ρ_{xx} and ρ_{xy} versus B in this range is shown in Fig. 3a. Here, the oscillation in ρ_{xx} is labelled by the filling factor ν ($\nu = 1, 2, 3, 4\ldots$), with values extracted from the Landau-level fan diagram. (This $1/B$ periodicity is also observed in $d\rho_{xy}/dB$ versus $1/B$, as shown in Fig. 3f.) There are several key observations. First, the extreme quantum limit that goes below $\nu = 1$ is achieved in ZrTe$_5$ at a very small field of about 1.3 T, much lower than most quantum Hall systems studied until now. Second, there appears to be a clear correlation between ρ_{xx} and ρ_{xy}: the dips in ρ_{xx} correspond to relatively flat plateaus in ρ_{xy}, and the peaks in ρ_{xx} correspond to the transition regions between the plateaus in ρ_{xy}. Last, and most remarkable, is that after entering the extreme quantum limit, the last dip in ρ_{xx} becomes vanishingly small, $\rho_{xx} \approx 0$, in a range of B fields around 2 T, accompanying a well-developed plateau in ρ_{xy}, and $\rho_{xy} \gg \rho_{xx}$. This is exactly the hallmark of the 3D QHE predicted by Halperin[3].

It must be pointed out that for the QHE observed here, the system bandwidth W_z ($W_z \approx 400$ meV)[12] is much larger than the Fermi energy E_F and the Landau level spacing (both about 25 meV). Hence, the QHE observed in our experiment is indeed of 3D nature, distinct from quasi-2D systems consisting of weakly coupled 2D QHE layers.

To understand the origin of ρ_{xy} plateaus, we note that the value of the Hall resistance $R_{xy} = \rho_{xy}/d$ on the plateau (for example, $R_{xy} \approx 1.35$ Ω, with a thickness of $d \approx 110$ μm for sample 2) is much smaller than the Klitzing constant $h/e^2 \approx 25.812$ kΩ by a factor of about 10^{-4}, indicating that the effect originates from the bulk, rather than from the 2D surfaces. From equation (1), the corresponding expression for the Hall resistivity is $\rho_{xy} = \frac{h}{e^2}\lambda_Q$, where λ_Q is the period of the system in real space (possibly divided by an integer number), and can be extracted from the measured plateau value of ρ_{xy}. For sample 2, $\lambda_Q \approx 5.8$ nm. Evidently, the period λ_Q is much larger than the lattice constant along z (about 1.45 nm), so the energy gap cannot be explained as arising from the lattice potential.

A key observation is that the value of λ_Q is close to half of $\lambda_{F,z}$, the Fermi wavelength along z. Surprisingly, this observation applies to all samples. In Fig. 3b, we plot the values of λ_Q and $\lambda_{F,z}$ for the four samples. Although λ_Q and $\lambda_{F,z}$ vary (mainly owing to the variation in carrier density), all the data points are sitting close to the straight line $\lambda_Q = \lambda_{F,z}/2$. Because the wavelength $\lambda_{F,z}/2$ corresponds to a wave-vector

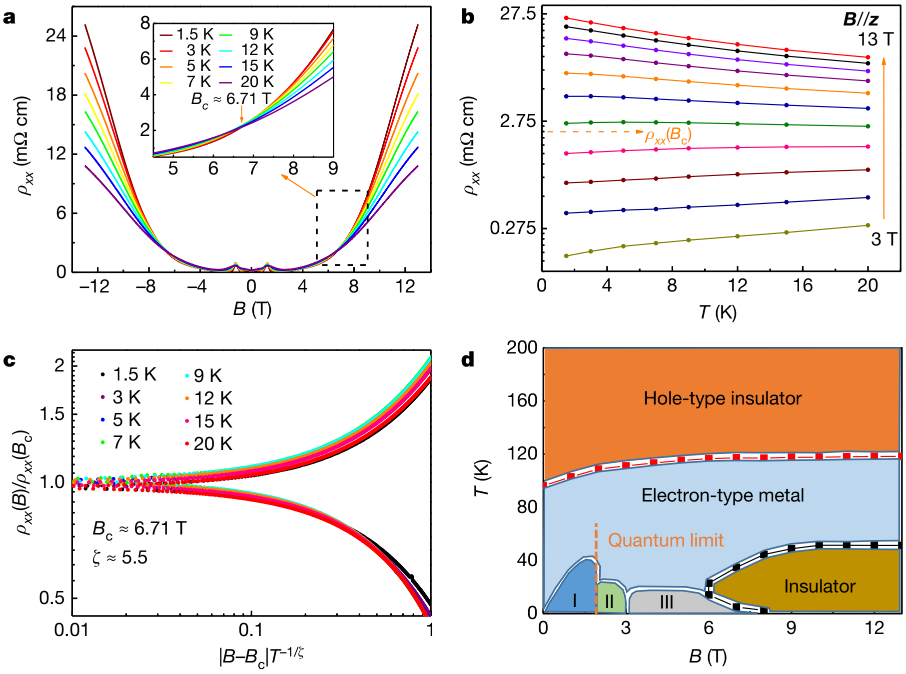

Fig. 4 | Metal–insulator transition and phase diagrams. a, Longitudinal resistivity $\rho_{xx}(B)$ versus magnetic field B at different temperature T ranging from 1.5 K to 20 K. The inset shows a zoom-in image around the critical (or crossover) point, where the critical resistivity is $\rho_{xx}(B_c)$ at a magnetic field of B_c. **b**, $\rho_{xx}(B)$ versus temperature T with the magnetic field B varying from 3 T to 13 T. **c**, Normalized resistivity $\rho_{xx}(B)/\rho_{xx}(B_c)$ as a function of scaling parameter $|B-B_c|T^{-1/\zeta}$. **d**, Phase diagram summarizing our results. See main text for discussion.

of $2k_{F,z}$—namely, the span of the Fermi surface along z—the strong correlation between λ_Q and half of $\lambda_{F,z}$ clearly points to a Fermi surface instability. Indeed, it has been long believed that a strong magnetic field can drive various Fermi surface instabilities for a 3D electron gas. The applied $\boldsymbol{B}$ field quantizes the electron motion in the plane perpendicular to the field, suppressing the in-plane kinetic energy, whereas the motion along the field is not affected, thus making the system behave as a quasi-1D (one-dimensional) system. The original 3D band structure is turned into the 1D Landau band spectrum with only k_z dispersion (as illustrated in Fig. 3c). With a sufficiently strong field (here about 1.3 T), the system enters the extreme quantum limit, where only the lowest ($N = 0$) Landau level is occupied, and the Fermi surface becomes only two points with perfect Fermi surface nesting. It is well known that such quasi-1D systems possess pronounced Fermi surface instabilities driven by interaction effects towards various insulating phases, such as charge-density wave (CDW), spin-density wave (SDW) and excitonic insulator states[19,20]. For our case, there is only a single electron pocket, and the lowest Landau level has no spin degeneracy[21] (owing to both Zeeman splitting and strong spin–orbit coupling), hence the SDW and excitonic insulator states are unlikely. The only reasonable candidate is therefore a CDW state. In such a CDW state, one expects periodic electron density modulation along the z direction, with a period corresponding to a nesting wave-vector close to $2k_{F,z}$ right after entering the extreme quantum limit, which is in good agreement with the experimental observation.

Our result, therefore, indicates an interaction-driven 3D QHE. Here, the interaction effects are enhanced by several factors. One is the Landau quantization, which effectively reduces the dimensionality of the electronic system. The second is the ease in achieving the extreme quantum limit owing to the low carrier density and single electron pocket, where perfect Fermi surface nesting can be realized. The third is the structural anisotropy, which results in relatively small dispersion along z (but the system is still 3D, not quasi-2D).

Moreover, we note that ρ_{xx} approaches zero only in a small interval of field strength—for example, 1.7–2.2 T for sample 2—and starts to increase upon further increasing the B field. This indicates that the CDW state survives only over a limited range of B values. The wave-vector $k_{F,z}$ in the extreme quantum limit should depend on B because the Landau level degeneracy is proportional to B. Hence, in the simplest picture, the period of the CDW state λ_Q—and hence ρ_{xy}—would be field-dependent, which apparently contradicts the relatively flat plateau that is observed. These observations can be reconciled by noticing that the values of λ_Q are close to integer multiples of the interlayer spacing along z (recall that there are two layers per unit cell, and the interlayer distance is about 0.725 nm); for samples 1, 2, 3 and 4, these values are within an error equal to 4, 8, 7 and 7 times the layer spacing, respectively (see Extended Data Table 2). Given the layered structure in the z direction, it is reasonable that such commensurate CDW states are more stable than incommensurate states[22,23], and once a commensurate CDW state is formed, it is usually pinned by the interaction with the lattice for a range of magnetic-field strengths. Further evidence of the field-induced CDW state comes from nonlinear transport[24,25] along z, for which one expects a non-Ohmic behaviour arising from a sliding CDW state when the applied bias voltage or current reaches the depinning threshold. This has indeed been observed in our experiment (see Supplementary Information).

In Fig. 3d, we plot the angular dependence of the Hall resistivity $\rho_{xy}(B)$. By changing β, we find that the quantization values of $\rho_{xy}(B)$ are consistent with about $\frac{h}{e^2}\frac{\lambda_{F,z}}{2}$. Similar results are obtained for $\alpha < 70°$, where $\rho_{xy}(B)$ depends only on the perpendicular component of the field, $B_\perp = B\cos\beta$ (or α). Figure 3e shows the temperature dependence of $\rho_{xy}(B)$, and one observes that the plateaus of $\rho_{xy}(B)$ survive even at $T = 15$ K (also see Extended Data Figs. 1, 2).

To better visualize the quantization features, we plot $\mathrm{d}\rho_{xy}/\mathrm{d}B$ (or $-\mathrm{d}^2\rho_{xx}/\mathrm{d}B^2$; see Supplementary Information) as a function of $1/B_\perp$ (Fig. 3f). The pronounced peaks are periodic in $1/B_\perp$ and are consistent for different angles and temperatures. Then, one clearly finds the positions of peaks corresponding to the filling factor $\nu = 1$–5. With this identification, one also notes a peak corresponding to the fractional filling factor $\nu = 1/3$ for all four samples (see Extended Data Fig. 3). The correspondence of this peak with a fraction of the Landau index is striking, and this signature provides a possible precursor for exploring the Laughlin type of 3D fractional quantum Hall states in future works.

Next, we explore transport at even higher fields. Figure 4a shows measurements up to 13 T with the temperature varying from 1.5 K to 20 K. One observes that $\rho_{xx}(B)$ stops oscillating at $B > 3$ T and increases rapidly without any sign of saturation, achieving a colossal magnetoresistance—higher than 15,000%—at 13 T. Strikingly, when plotting $\rho_{xx}(B)$ curves measured at different temperatures together, one finds that all the curves share a common crossing point at a critical magnetic field of $B_c = 6.71$ T. We also plot ρ_{xx} as a function of T, with B varying from 2 T to 13 T in Fig. 4b. One finds that ρ_{xx} monotonically increases as T drops in the region above B_c, as expected for an insulator. This feature clearly signals a critical point for a metal–insulator transition: the system is metallic below B_c and insulating above B_c.

Typically, for magnetic-field-induced metal–insulator transitions, the isotherms of ρ_{xx} have a universal scaling with the parameter $(B-B_c)T^{-1/\zeta}$. In Fig. 4c, we perform such a scaling analysis, and indeed all the isotherms fall onto a single curve as a function of $|B-B_c|T^{-1/\zeta}$, with a fitted critical exponent of $\zeta \approx 5.5$.

We are unable to determine the nature of the insulating state above B_c at present. There are at least two possibilities. The first is the formation of Wigner crystals. We note that the values of B_c correspond to the critical filling factors $\nu_c \approx 0.182, 0.173, 0.193$ for samples 1, 2, 3, respectively, which are all below 1/5. This is consistent with the common belief[26–28] that Wigner crystals form below the critical filling factor of 1/5. The second possibility is localization due to impurities and defects[29,30]. For our high-quality samples, the main source of defects is the dopants. The Landau orbital size would become progressively smaller with increasing magnetic field, leading to carrier localization on these defects.

We summarize our findings with a phase diagram in the B–T plane, shown in Fig. 4d. First, from Fig. 1c, we identify a hole-type insulating state at $T > T_p$, which is converted to electron-type metallic states at $T < T_p$. In the presence of a magnetic field, Landau quantization leads to CDW states or other Fermi surface instabilities in region I at low temperatures; this region may actually host a sequence of 3D integer QHEs that we have evidence for, but are unable to establish owing to the finite ρ_{xx}. In region II (extreme quantum limit), we have clear evidence of a 3D QHE with CDW formation. We see a signature suggesting a 3D $\nu_c = 1/3$ fractional quantum Hall state in region III. Finally, we find a metal–insulator transition with further increasing B. We note that this is a zero-temperature (quantum) phase transition, which needs to be explored further in the future. The finite-T boundaries separating metallic and insulating phases, on the other hand, represent crossovers.

Online content

Any methods, additional references, Nature Research reporting summaries, source data, statements of data availability and associated accession codes are available at https://doi.org/10.1038/s41586-019-1180-9.

Received: 3 July 2018; Accepted: 12 February 2019;
Published online 8 May 2019.

1. Klitzing, K. v., Dorda, G. & Pepper, M. New method for high-accuracy determination of the fine-structure constant based on quantized Hall resistance. *Phys. Rev. Lett.* **45**, 494–497 (1980).
2. Tsui, D. C., Stormer, H. L. & Gossard, A. C. Two-dimensional magnetotransport in the extreme quantum limit. *Phys. Rev. Lett.* **48**, 1559–1562 (1982).
3. Halperin, B. I. Possible states for a three-dimensional electron gas in a strong magnetic field. *Jpn. J. Appl. Phys.* **26**, 1913–1919 (1987).
4. Kohmoto, M., Halperin, B. I. & Wu, Y.-S. Diophantine equation for the three-dimensional quantum Hall effect. *Phys. Rev. B* **45**, 13488–13493 (1992).
5. Bernevig, A., Hughes, T., Raghu, S. & Arovas, D. Theory of the three-dimensional quantum Hall effect in graphite. *Phys. Rev. Lett.* **99**, 146804 (2007).
6. Störmer, H. L., Eisenstein, J. P., Gossard, A. C., Wiegmann, W. & Baldwin, K. Quantization of the Hall effect in an anisotropic three-dimensional electronic system. *Phys. Rev. Lett.* **56**, 85–88 (1986).
7. Hannahs, S. T., Brooks, J. S., Kang, W., Chiang, L. Y. & Chaikin, P. M. Quantum Hall effect in a bulk crystal. *Phys. Rev. Lett.* **63**, 1988–1991 (1989).
8. Cooper, J. R. K., Auban, W., Montambaux, P. & Jérome, G. D. & Bechgaard, K. Quantized Hall effect and a new field-induced phase transition in the organic superconductor (TMTSF)$_2$(PF)$_6$. *Phys. Rev. Lett.* **63**, 1984–1987 (1989).
9. Hill, S. et al. Bulk quantum Hall effect in η–Mo$_4$O$_{11}$. *Phys. Rev. B* **58**, 10778–10783 (1998).
10. Cao, H. et al. Quantized Hall effect and Shubnikov–de Haas oscillations in highly doped Bi$_2$Se$_3$: evidence for layered transport of bulk carriers. *Phys. Rev. Lett.* **108**, 216803 (2012).
11. Masuda, H. et al. Quantum Hall effect in a bulk antiferromagnet EuMnBi$_2$ with magnetically confined two-dimensional Dirac fermions. *Sci. Adv.* **2**, e1501117 (2016).
12. Weng, H., Dai, X. & Fang, Z. Transition-metal pentatelluride ZrTe$_5$ and HfTe$_5$: a paradigm for large-gap quantum spin Hall insulators. *Phys. Rev. X* **4**, 011002 (2014).
13. Jones, T. E., Fuller, W. W., Wieting, T. J. & Levy, F. Thermoelectric power of HfTe$_5$ and ZrTe$_5$. *Solid State Commun.* **42**, 793–798 (1982).
14. Li, Q. et al. Chiral magnetic effect in ZrTe$_5$. *Nat. Phys.* **12**, 550–554 (2016).
15. Liang, T. et al. Anomalous Hall effect in ZrTe$_5$. *Nat. Phys.* **14**, 451–455 (2018).
16. Liu, Y. et al. Zeeman splitting and dynamical mass generation in Dirac semimetal ZrTe$_5$. *Nat. Commun.* **7**, 12516 (2016).
17. Zheng, G. et al. Transport evidence for the three-dimensional Dirac semimetal phase in ZrTe$_5$. *Phys. Rev. B* **93**, 115414 (2016).
18. Zhang, Y. et al. Electronic evidence of temperature-induced Lifshitz transition and topological nature in ZrTe$_5$. *Nat. Commun.* **8**, 15512 (2017).
19. Bardasis, A. & Das Sarma, S. Peierls instability in degenerate semiconductors under strong external magnetic fields. *Phys. Rev. B* **29**, 780–784 (1984).
20. MacDonald, A. & Bryant, G. Strong-magnetic-field states of the pure electron plasma. *Phys. Rev. Lett.* **58**, 515–518 (1987).
21. Chen, R. Y. et al. Magnetoinfrared spectroscopy of Landau levels and Zeeman splitting of three-dimensional massless Dirac fermions in ZrTe$_5$. *Phys. Rev. Lett.* **115**, 176404 (2015).
22. Wilson, J. A., Di Salvo, F. J. & Mahajan, S. Charge-density waves and superlattices in the metallic layered transition metal dichalcogenides. *Adv. Phys.* **24**, 117 (1975).
23. McMillan, W. L. Theory of discommensurations and the commensurate–incommensurate charge-density-wave phase transition. *Phys. Rev. B* **14**, 1496 (1976).
24. Lee, P. A. & Rice, T. M. Electric field depinning of charge density waves. *Phys. Rev. B* **19**, 3970 (1979).
25. Monçeau, P., Ong, N. P., Portis, A. M., Meerschaut, A. & Rouxel, J. Electric field breakdown of charge-density-wave–induced anomalies in NbSe$_3$. *Phys. Rev. Lett.* **37**, 602 (1976).
26. Andrei, E. et al. Observation of a magnetically induced Wigner solid. *Phys. Rev. Lett.* **60**, 2765–2768 (1988).
27. Zhang, C., Du, R.-R., Manfra, M. J., Pfeiffer, L. N. & West, K. W. Transport of a sliding Wigner crystal in the four flux composite fermion regime. *Phys. Rev. B* **92**, 075434 (2015).
28. Yang, K., Haldane, F. D. M. & Rezayi, E. H. Wigner crystals in the lowest Landau level at low-filling factors. *Phys. Rev. B* **64**, 081301 (2001).
29. Field, S. B., Reich, D. H., Rosenbaum, T. F., Littlewood, P. B. & Nelson, D. A. Electron correlation and disorder in Hg$_{1-x}$Cd$_x$Te in a magnetic field. *Phys. Rev. B* **38**, 1856–1864 (1988).
30. Shayegan, M., Goldman, V. J. & Drew, H. D. Magnetic-field-induced localization in narrow-gap semiconductors Hg$_{1-x}$Cd$_x$Te and InSb. *Phys. Rev. B* **38**, 5585–5602 (1988).

Acknowledgements We thank J. Mei, L. Fu, X. Dai, X. Wang, K. T. Law, D. Yu, F. Zhang, J. Wu and D. L. Deng for valuable discussions. This work was supported by the Guangdong Innovative and Entrepreneurial Research Team Program (2016ZT06D348), NNSFC (11874193), the Shenzhen Fundamental Subject Research Program (JCYJ20170817110751776) and the Innovation Commission of Shenzhen Municipality (KQTD2016022619565991). F.T. thanks the Department of Physics, Renmin University of China for visiting student support. Work at the University of Science and Technology of China, was supported by the National Key R&D Program of China (2016YFA0301700), NNSFC (11474265) and Anhui Initiative in Quantum Information Technologies (AHY170000). Work at Brookhaven is supported by the Office of Basic Energy Sciences, US Department of Energy under contract number DE-SC0012704. The work of K.Y. is supported by National Science Foundation grants DMR-1442366 and DMR-1644779. P.A.L. acknowledges support by the US Department of Energy Basic Energy Sciences grant DE-FG02-03-ER46076. S.A.Y. is supported by the Singapore Ministry of Education AcRF Tier 2 (MOE2015-T2-2-144).

Reviewer information *Nature* thanks Alberto Crepaldi, Itamar Kimchi and the other anonymous reviewer(s) for their contribution to the peer review of this work.

Author contributions F.T. and P.W. carried out the transport measurements. J.S., R.Z. and G.G. prepared the samples. Y.R., S.A.Y., K.Y. and P.A.L. performed the theoretical analysis. Z.Q. and L.Z. designed and supervised the work. All authors contributed to the interpretation and analysis of the data and the writing of the manuscript.

Competing interests The authors declare no competing interests.

Additional information
Extended data is available for this paper at https://doi.org/10.1038/s41586-019-1180-9.
Supplementary information is available for this paper at https://doi.org/10.1038/s41586-019-1180-9.
Reprints and permissions information is available at http://www.nature.com/reprints.
Correspondence and requests for materials should be addressed to S.A.Y., Z.Q. or L.Z.

METHODS

Sample synthesis and characterization. High-quality single-crystal $ZrTe_5$ was synthesized with high-purity elements (99.9999% zirconium and 99.9999% tellurium), and needle-like crystals (about $0.1 \times 0.3 \times 20$ mm^3) were obtained by the tellurium flux method and chemical vapour transport. The lattice parameters of the crystals were structurally confirmed by X-ray diffraction, scanning tunnelling microscopy and transmission electron microscopy with electron diffraction. The low-temperature magneto-transport measurements were performed in an Oxford TeslatronPT cryostat with a variable temperature range of 1.5–300 K and a rotatable probe insert with angles of 0–290°, or in a ^{3}He probe insert with a base temperature of 260 mK, and a superconductor magnetic field of up to 14 T. In all our measurements, the current I (10–100 μA) was applied along an axis, and the four-terminal resistance was measured using the standard lock-in method with a low frequency (17.777 Hz). The magnetic field was rotated from the z axis to both the x and y axes to measure the anisotropy. The bulk carrier density $n \approx 10^{16}$ cm^{-3} was obtained from the Hall effect measurements at low magnetic field and also from the analysis of SdH oscillations.

Distinguishing 3D and quasi-2D systems. In terms of electronic properties, quasi-2D and 3D systems are distinguished by their Fermi surface topology: the Fermi surface of a quasi-2D system is open along the stacking direction (owing to the small interlayer coupling), whereas the Fermi surface of a 3D system is closed, although it may be highly anisotropic.

A simple criterion is to compare two energy scales: the bandwidth W_z and the Fermi energy E_F. If $W_z < E_F$, the system is quasi-2D; otherwise, it is 3D. For 3D QHE, we further need a W_z value larger than the Landau level spacing. Such topological distinction has clear experimental indications in magnetic quantum oscillations, such as SdH oscillations. For a 3D system, owing to its closed Fermi surface, quantum oscillations occur for a $\boldsymbol{B}$ field oriented along arbitrary directions. By contrast, for a quasi-2D system, a closed orbit cannot form along the (stacking) direction in which the Fermi surface is open, hence quantum oscillation cannot appear for an in-plane-oriented $\boldsymbol{B}$ field (see Extended Data Fig. 4). This difference in quantum oscillation behaviour offers a clear criterion for distinguishing 3D from quasi-2D systems (more discussion is provided in Supplementary Information).

Data availability

The data that support the findings of this study are available from the corresponding author on request.

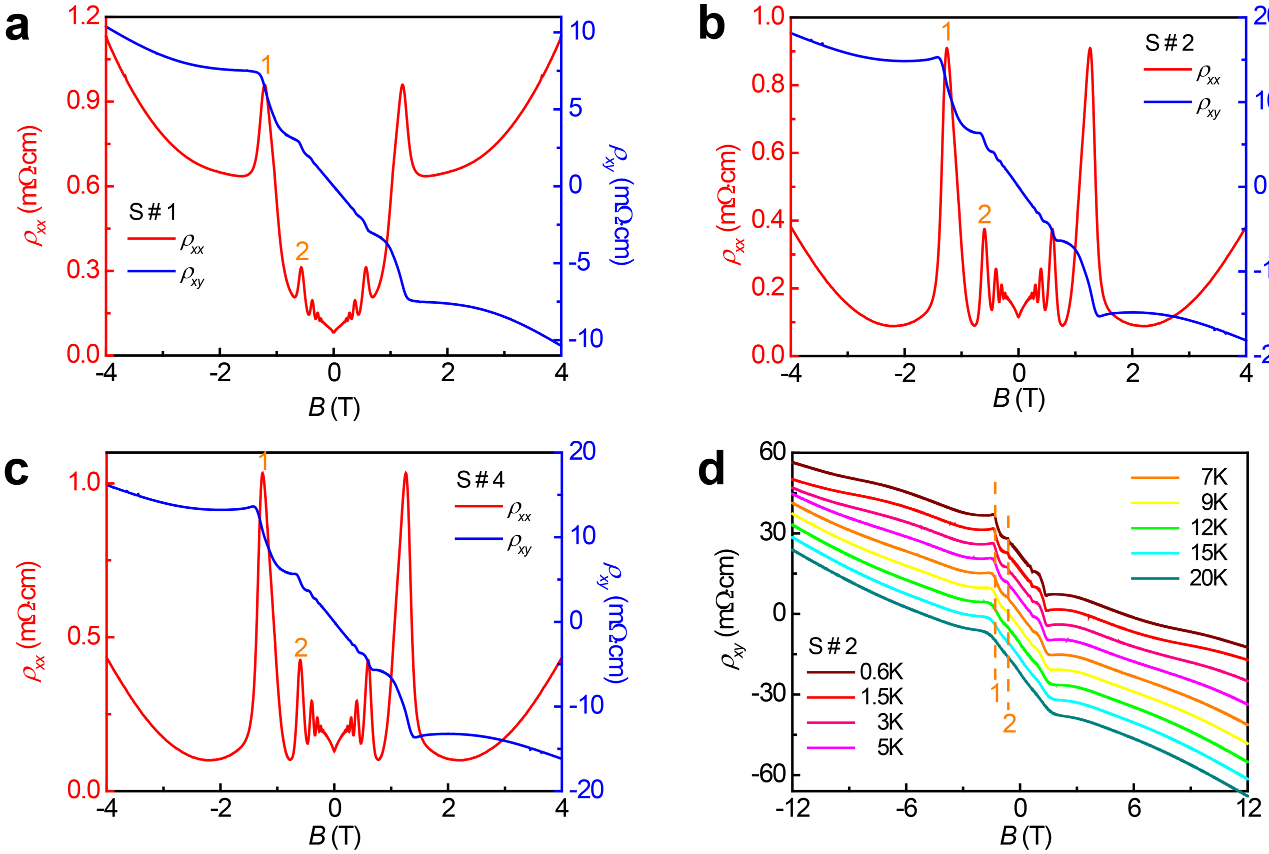

Extended Data Fig. 1 | 3D QHE in different samples and temperature dependence of Hall resistivity. a–c, 3D QHE results for ZrTe$_5$ samples 1 (**a**), 2 (**b**) and 4 (**c**) at $T = 1.5$ K. **d**, Hall resistivity of sample 2 at different temperatures ranging from 0.6 K to 20 K. Neighbouring curves are shifted by 5 mΩ cm for clarity.

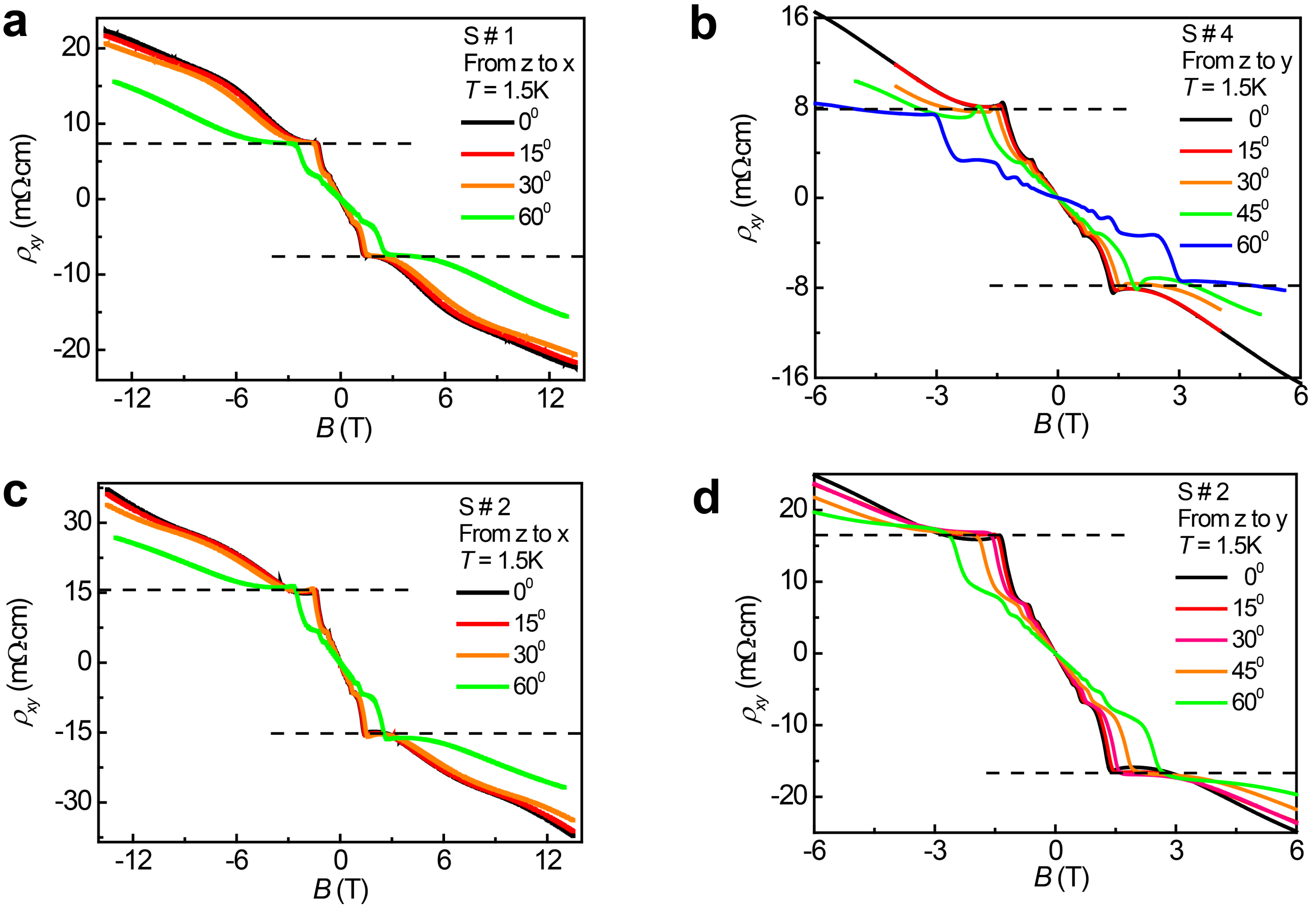

Extended Data Fig. 2 | Angular dependence of Hall resistivity. a–d, The dependence of the Hall resistivity on angle β (**a**, **c**) and angle α (**b**, **d**) is shown for $ZrTe_5$ samples 1 (**a**), 4 (**b**), 2 (**c**) and 2 (**d**).

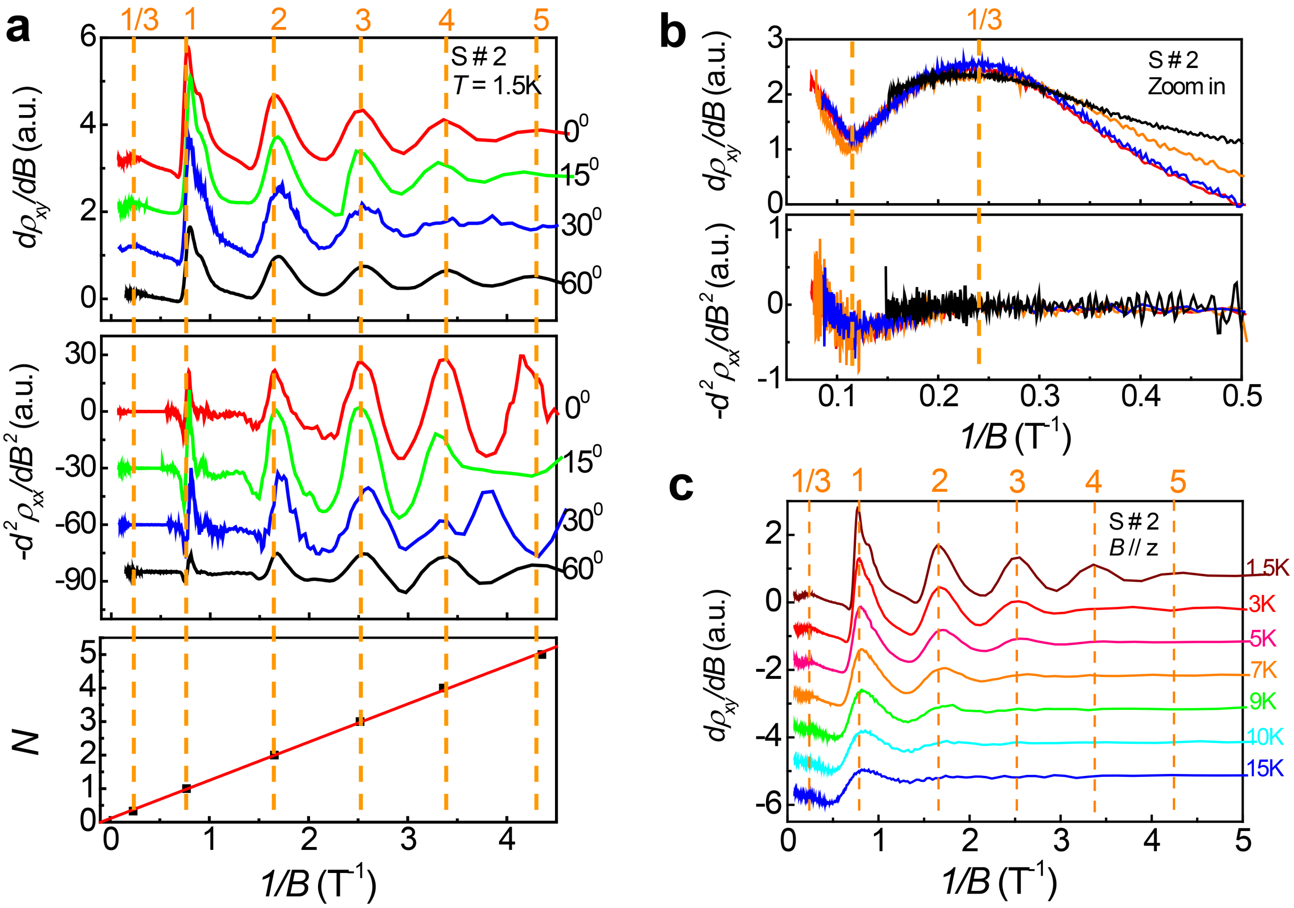

Extended Data Fig. 3 | Signatures of 3D fractional QHE. **a**, dρ_{xy}/dB and $-$d$^2\rho_{xx}$/dB^2 and versus 1/$B_\perp$ at angles $\beta = 0°$, 15°, 30°, 60°. The vertical dashed lines indicate the $N = 1/3$, 1, 2, 3, 4, 5 Landau indices. **b**, Zoom-in of the extreme-quantum-limit region $0 < N < 1$. The $N = 1/3$ peak can be observed. **c**, dρ_{xy}/dB versus 1/$B_\perp$ at temperatures ranging from 1.5 K to 15 K.

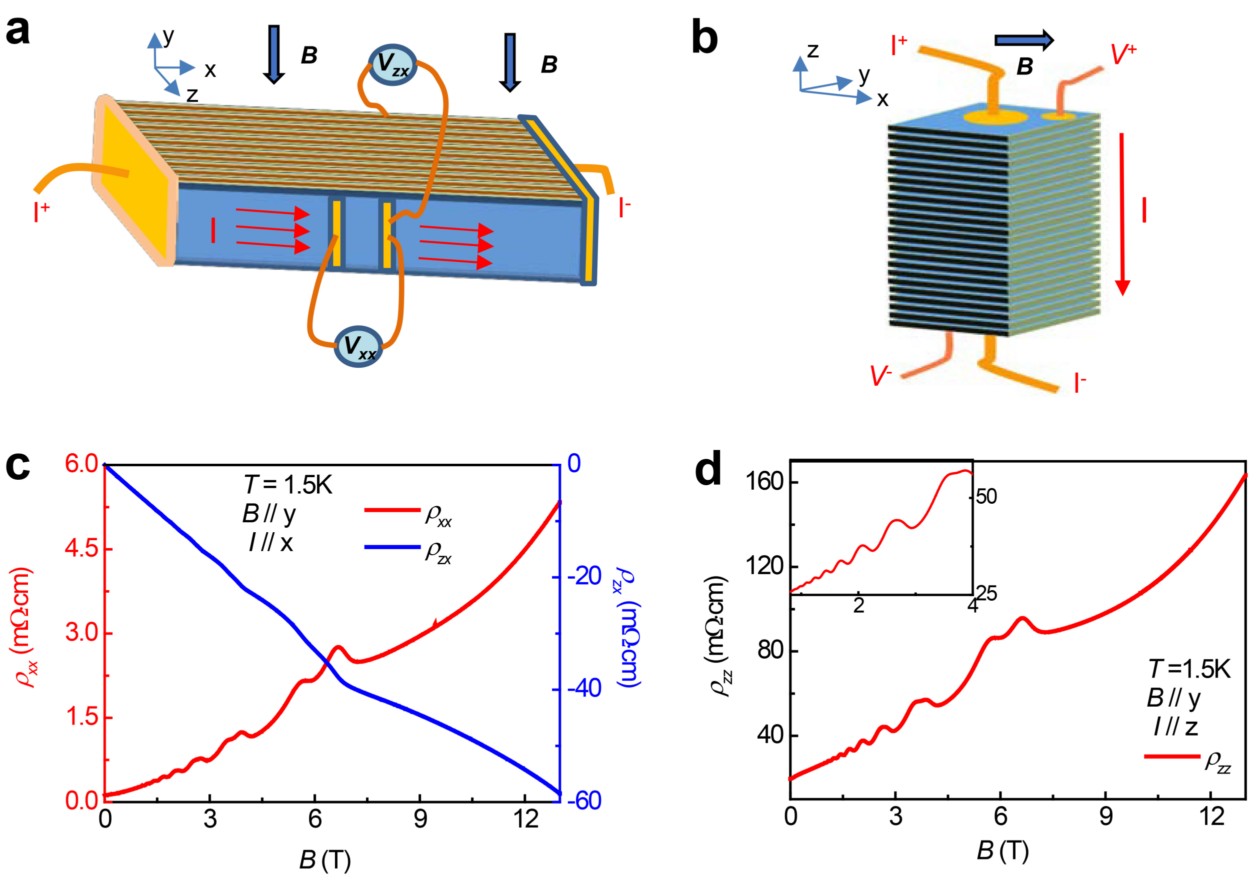

Extended Data Fig. 4 | In-plane measurements and quantum oscillations. Measurement of SdH oscillations in $ZrTe_5$ (sample 4) when a magnetic field is applied in the y direction. **a**–**d**, Coherent transport of ρ_{xx} (**a**, **c**) and ρ_{zz} (**b**, **d**). **a**, **b**, Schematic illustration of the setup with $\boldsymbol{B}//\boldsymbol{y}$ and $\boldsymbol{I}//\boldsymbol{x}$ (**a**) and with $\boldsymbol{B}//\boldsymbol{y}$ and $\boldsymbol{I}//\boldsymbol{z}$ (**b**). **c**, Longitudinal resistivity ρ_{xx} and Hall resistivity ρ_{zx} measured in the x–z plane, with magnetic field $\boldsymbol{B}//\boldsymbol{y}$ and current $\boldsymbol{I}//\boldsymbol{x}$. **c**, **d**, ρ_{xx} and ρ_{zz} show similar oscillation patterns. Inset, zoom-in view of ρ_{zz} versus $\boldsymbol{B}$. However, in zero magnetic field, the resistivity ρ_{zz} is about 30 times larger than ρ_{xx}.

Extended Data Table 1 | Charge-transport parameters

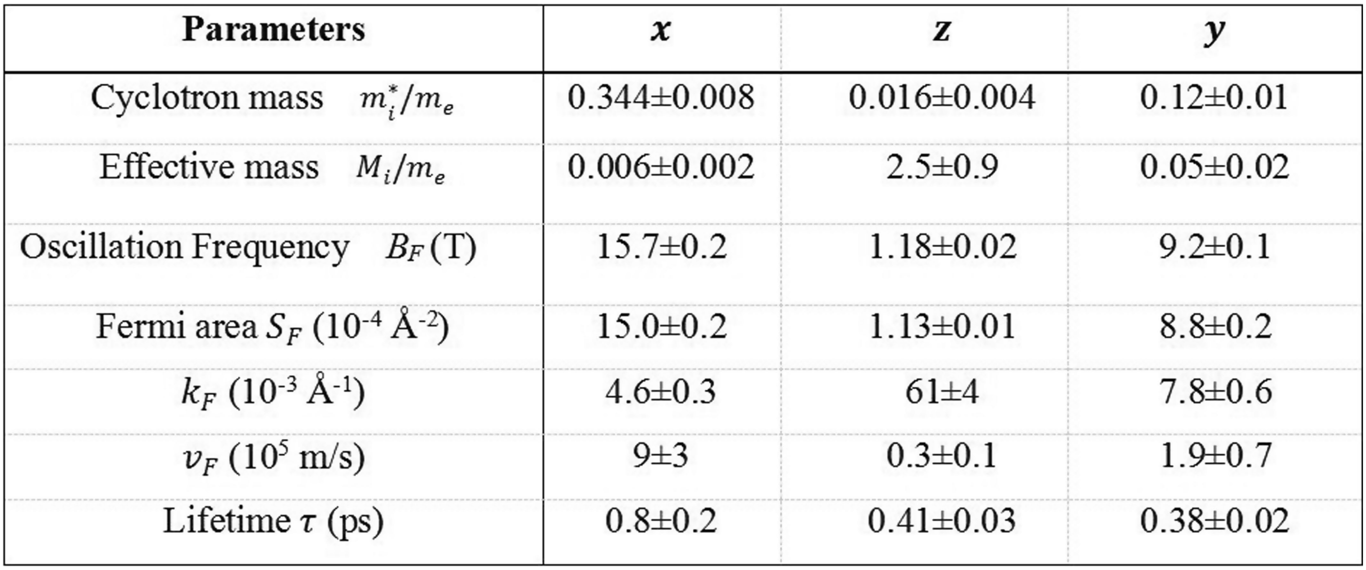

Parameters	***x***	***z***	***y***
Cyclotron mass m_i^*/m_e	0.344±0.008	0.016±0.004	0.12±0.01
Effective mass M_i/m_e	0.006±0.002	2.5±0.9	0.05±0.02
Oscillation Frequency B_F (T)	15.7±0.2	1.18±0.02	9.2±0.1
Fermi area S_F (10^{-4} Å^{-2})	15.0±0.2	1.13±0.01	8.8±0.2
k_F (10^{-3} Å^{-1})	4.6±0.3	61±4	7.8±0.6
v_F (10^5 m/s)	9±3	0.3±0.1	1.9±0.7
Lifetime τ (ps)	0.8±0.2	0.41±0.03	0.38±0.02

Anisotropic transport parameters along different directions for sample 2.

Extended Data Table 2 | Fermi wavelength $\lambda_{F,z}$ and CDW period λ_Q for different samples

Sample	S#1	S#2	S#3	S#4
$\lambda_{F,z}$ (nm)	5.40±0.03	11.30±0.07	9.3±0.3	10.2±0.2
λ_Q (nm)	3.1±0.5	5.9±0.6	5±1	5.2±0.5
$\lambda_Q/\lambda_{F,z}$	0.57±0.09	0.52±0.05	0.5±0.1	0.51±0.06
$\lambda_Q/(7.25Å)$	4.2±0.4	8.1±0.8	6.9±1.4	7.2±0.8